Effects of decarbonation on elemental behaviors during subduction-zone metamorphism: Evidence from a titanite-rich contact between eclogite-facies marble and omphacitite

Yuanyuan Xiao [1, 2, 3, *], Yaoling Niu [1, 2, 4], Hong-Fu Zhang [5, 6], Kuo-Lung Wang [3], Yoshiyuki Iizuka [3], Jinyan Lin [5], Yulong Tan [5], Yongjiang Xu [5]

[1] Institute of Oceanology, Chinese Academy of Sciences, Qingdao, 266071, China

[2] Laboratory for Marine Geology, Qingdao National Laboratory for Marine Science and Technology, Qingdao 266061, China

[3] Institute of Earth Sciences, Academia Sinica, Taipei, 11529, Taiwan

[4] Department of Earth Sciences, Durham University, Durham, DH1 3LE, UK

[5] Department of Geology, Northwest University, Xi'an, 710069, China

[6] State Key Laboratory of Lithospheric Evolution, Institute of Geology and Geophysics, Chinese Academy of Sciences, Beijing, 100029, China

*Corresponding author:

Dr Yuanyuan XIAO. Telephone: +86-0532-82898035. E-mail: yuanyuan_xiao@foxmail.com.

Abstract

In this paper, we show the effects of subducted carbonates on geochemical processes during subduction-zone metamorphism (SZM) through the study of an eclogite-facies marble coexisting with metabasite from the ultrahigh pressure metamorphic belt of the Chinese Western Tianshan orogen. Between the marble and metabasite is a titanite-rich contact resulting from fluid-facilitated metamorphic reactions between the two lithologies, and recording elemental changes of geodynamic significance. Because this titanite-rich contact is dominated by titanite (an important host for high field strength elements, HFSEs) without white micas (an important host for large ion lithophile elements, LILEs), HFSEs are largely conserved in titanite whereas LILEs are moved away. This observation emphasizes the potential significance of subducting carbonate in retaining HFSEs in the slab through the formation and stabilization of titanite, contributing to the characteristic "arc signature" unique to subduction-zone magmatism (i.e., high LILEs, low HFSEs). The implicit assumption in this interpretation is that the observed lithological assemblage represents residues of subducting oceanic crust that has undergone major episodes of dehydration. Subducted carbonates also have significant implications for the origin of mantle isotopic heterogeneity as revealed from oceanic basalts.

Key words: marine carbonate subduction, behaviors of chemical elements, subduction-zone metamorphism, subduction-zone magmatism, mantle isotopic heterogeneity

1 Introduction

Arc magmas with characteristic “arc” signatures (i.e., high large ion lithophile elements, LILEs and low high field strength elements, HFSEs) have been interpreted as resulting from slab dehydration-induced mantle wedge peridotite melting (“fluid-flux melting”; McCulloch and Gamble, 1991). The released fluids are thought to selectively carry water-soluble (or mobile) elements (e.g., Ba, Rb, Cs, K, Sr, Pb, U, B, As, Sb) into the mantle wedge, while the water-insoluble (or immobile) elements (e.g., HFSEs, heavy rare earth elements [HREEs]) remain in the subducting slab carried further into the deep mantle (McCulloch and Gamble, 1991). Therefore, to understand behaviors of chemical elements during subduction-zone metamorphism (SZM) is important for better understanding arc magmatism. We have a good understanding of elemental behaviors during SZM on hand-specimen and even meter-scales, which are largely controlled by the formation and stability of relevant element-hosted minerals (El Korh et al., 2009; Hermann and Rubatto, 2009; Beinlich et al., 2010; Xiao et al., 2012, 2013, 2014, 2016). The abundances of fluids and fluid properties (e.g., fluids with dissolved Na-Al silicates or halogen, supercritical fluids above the second critical point) can also control the elemental mobility (Gao and Klemd, 2001; Rubatto and Hermann, 2003; Gao et al., 2007; Zack and John, 2007; John et al., 2008).

Despite all these complexities, we cannot truly understand geochemical behaviors of chemical elements during SZM without evaluating the effects of subducting/subducted carbonate. Carbonate makes up to ~ 7 wt.% of the global subducting sediments (GLOSS; Plank and Langmuir, 1998), and can indeed subduct

mixed with silicate sediments and altered oceanic crust. As a result, carbonation and decarbonation readily happen during metamorphism (Niu and Lesher, 1992). Hence, subducting/subducted carbonate must participate in metamorphic reactions and is likely to influence geochemical processes during SZM most likely in the form of CO_2. The significance of subducting/subducted carbonate has been discussed in the context of global carbon recycling (Kerrick and Connolly, 2001a,b; Caciagli and Manning, 2003; Hayes and Waldbauer, 2006; Huybers and Langmuir, 2009; Manning et al., 2013; Ague and Nicolescu, 2014; Flesia and Frezzotti, 2015; Liu et al., 2015; Thomson et al., 2016) and the petrogenesis of mantle carbonatite and related mantle metasomatism (Yaxley and Brey, 2004; Dasgupta and Hirschmann, 2006, 2010; Tsuno et al., 2012; Poli, 2015).

In this paper, we report our findings of a titanite-rich contact between the marble and metabasite formed as the result of reactions between the two lithologies during seafloor subduction recorded in the ultrahigh pressure (UHP) metamorphic assemblage of the Chinese Western Tianshan orogenic belt (Xiao et al., 2012; Lü et al., 2013). We discuss the geochemical significance of the titanite lithology in moderating elemental behaviors during SZM and the geodynamic implications of carbonate subduction.

2 Field Geology and Petrology

2.1 Field geology

The Chinese Western Tianshan orogenic belt has been confirmed to be a typical UHP metamorphic (UHPM) belt as evidenced by findings of coesite and coexisting magnesite and aragonite as the product of dolomite breakdown (Lü et al., 2008, 2009,

2013, 2014; Zhang et al., 2002a, b; Lü and Zhang, 2012). This UHPM belt represents a paleo-convergent margin associated with the successive northward subduction of the South Tianshan Silurian-Devonian-seafloor and the Tarim Plate in the Carboniferous (Fig. 1a; Gao et al., 1999; Gao and Klemd, 2003). In this UHPM belt, both metasedimentary rocks and metabasite coexist, including pelitic schist, marble, blueschist, and eclogite (Zhang et al., 2002a, b; Lü and Zhang, 2012; Lü et al., 2014). The protoliths of metabasite are oceanic basalts, including ocean island basalts (OIB), normal (N)-type and enriched (E)-type mid-ocean ridge basalts (MORB) as well as volcanic arc basalts (Gao and Klemd, 2003; Ai et al., 2006; Xiao et al., 2012).

Our study area is along the Atantayi River (Fig. 1b; Gao et al., 1999; Lü et al., 2014). Abundant marble is closely associated with other metasedimentary rocks (Figs. 2a,b; Lü et al., 2013) and metabasite (Figs. 2c,d). The marble intercalates with the metabasite, mica schist and mica quartz schist, the protolith of which are basaltic rocks, pelite and sandstone respectively. The marble shows well-preserved rhythmical interbeds with mica schist and mica quartz schist (Figs. 2a,c), probably inherited from the protolith assemblage of pelite, sandstone and carbonate as part of turbidite flysch sequence in a deep marine environment despite the subduction-exhumation related deformation (Fig. 2c). The marble also occurs as lenses together with the metabasite (Figs. 2a-c) with their long axes parallel to the orientation of other lithologies of the sequence (e.g., mica schist, mica quartz schist; Figs. 2a,b). The discrete carbonate and basaltic lenses (Figs. 2a-c) reflect disruption of turbidites by within-trench landslides. The entire sequence has experienced SZM. Our sample in this study (12TS-AT-18) is

from the contact between a metabasite enclave and the marble host (Fig. 2d).

2.2 Petrography

Between the marble (represented by circles 3 and 5-11 in Layer I; Figs. 3b-f) and metabasite (represented by circles 13-22 in Layer III-VI; Figs. 3i-l) is a titanite-rich contact (Figs. 3g,h; represented by circles 2, 4 and 12 in Layer II) with a large (~ 8 mm long) titanite crystal (Fig. 3a). The titanite-rich contact is dominated by well-crystallized titanite, clinozoisite (X_{Ps} ratios, $Fe^{3+}/[Fe^{3+}+Al]$, smaller than 0.05; Ps, pistacite; Supplementary Table S.1) and fine-grained aggregates of carbonate + omphacite + apatite (Fig. 3g; Layer II). (Sodic-)calcic amphibole is also occasionally present, replacing omphacite and clinozoisite. The elongation of titanite crystals is parallel to the contact between the marble and metabasite.

The marble (Layer I) is dominated by calcium carbonate (> 90 vol.%) with minor omphacite, epidote (with X_{Ps} ratio from 0.09 to 0.23, see Supplementary Table S.1), phengite (with Si atom per formula > 3.3), and paragonite (Figs. 3b-f, 4a-c). There is no reaction rim of these accessory minerals. Garnet is also present rimmed with epidote overgrowth (Figs. 3b, 4a). Only several tiny titanite inclusions are found in paragonite (Fig. 4c).

The metabasite consists mainly of clinozoisite (X_{Ps} ratios smaller than 0.05; Supplementary Table S.1), omphacite, amphibole (mainly sodic-calcic and calcic amphiboles with $Mg/[Mg+Fe^{2+}]$ ratios of 0.69 – 0.83), and titanite plus minor fine-grained paragonite and rare albite. Mineral modes (mainly omphacite and clinozoisite) vary significantly, and the metabasite can be further divided into omphacite-rich

(Layers IV & VI; Figs. 3j-l) and clinozoisite-rich (Layers III & V; Fig. 3i) parts. (Sodic-)calcic amphibole is present, replacing clinozoisite and omphacite. No carbonate mineral is observed in the metabasite. Large titanite crystals both from the metabasite and the titanite-rich contact have very-fine-grained residual rutile (Figs. 4d,e).

The occurrence of omphacite and garnet in the marble indicates that the marble has experienced eclogite-facies metamorphism as also evidenced by the close relationship of the marble with the omphacite-bearing metabasite. Epidote overgrown on the rim of the residual garnet (Figs. 3b,4a) results from the reaction between garnet and calcium carbonate during retrograde metamorphism.

3 Methods

Mineral compositions are analyzed in the Institute of Earth Sciences, Academia Sinica in Taipei. Mineral major elements are analyzed using a field emission scanning electron microscope (FE-SEM, JEOL JSM-7100F) equipped with an energy dispersive X-ray spectrometer (EDS, Oxford instruments Xmax 80) and a cathodoluminescence (CL) image detector (Deben Centaurus). The sample is carbon-coated and the analysis was done at an acceleration voltage of 15 kV with 0.1 nA current under the high vacuum environment ($<10^{-4}$ Pa) for 50 s in each run. The working distance is set at 10 mm. The X-ray intensities were corrected for using ZAF on synthetic mineral standards, i.e., wollastonite for Si and Ca, corundum for Al, fayalite for Fe, periclase for Mg, Cr oxide for Cr, InP (alloy) for P, rutile for Ti, Mn oxide (MnO_2) for Mn, albite for Na, and orthoclase for K. Analytical results of mineral major elements are given in

147 Supplementary Table S.1, and representative backscattered electron images (BSE) are
148 given in Fig. 4.

149 Mineral trace elements are analyzed using *in situ* Laser Ablation-Inductively
150 Coupled Plasma Mass Spectrometry (LA-ICP-MS, a ThermoFinnigan Element XR
151 equipped with Photon Machines Analyte G2 Excimer ArF 193 nm Laser sampler) on
152 polished thick (100 μm) "thin" sections. Si is chosen as the internal standard for trace
153 element analysis for all the minerals, but Ca is used for apatite. The repetition rate of
154 laser ablation is 5 Hz, and the spot size is 40 μm. In each run, acquisition times for the
155 background (gas blank) and the sample ablation are 45 s and 75 s respectively. The
156 energy fluence is 4.60 J/cm^2. The NIST (National Institute of Standards and Technology)
157 glass standard SRM 612 and the USGS (United States Geological Survey) glass
158 standard BCR-2G are analyzed as the reference materials. On the basis of repeated
159 analyses of BCR-2G, the accuracy is estimated to be within ± 10% for all the analyzed
160 elements but ~ 15% for Gd and Tb. The precision for all the analyzed trace elements is
161 better than 10% (Supplementary Table S.2). During the analysis, we purposely avoid
162 mineral inclusions. Analytical results of mineral trace elements are given in
163 Supplementary Table S.3.

164 ## 4 Results

165 In chondrite normalized trace element diagram (Fig. 5), the residual **garnet** with
166 epidote overgrowth (Figs. 3b,4a) shows highest HREE contents (10s ppm) with a
167 $(HREE > LREE)_{chondrite}$ pattern for all the analyzed grains (Fig. 5a). **Epidote** group
168 minerals show variably high contents of REEs (~ 1 – 10^3 times the chondritic values;

169 Fig. 5a). Epidote from the marble tends to show the highest REE contents than
170 clinozoisite from the titanite-rich contact or from the metabasite, e.g., up to 407 ppm
171 vs. 119 ppm for La (Supplementary Table S.3). The epidote overgrown on the rim of
172 the residual garnet from the marble displays the lowest LREEs (e.g., only several ppm
173 for La), Th and U (only 10s ppb vs. up to 10s ppm), but the highest HREEs (e.g., several
174 ppm vs. mostly < 1 ppm for Lu) among all the analyzed epidote group minerals (Fig.
175 5a).

176 All the **titanite** analyses show consistently high Nb and Ta contents, up to ~ 10^3 –
177 10^4 times the chondritic value (Fig. 5b). However, REE contents of titanite are highly
178 variable (from hundreds of ppb to 10s ppm), even within a single crystal grain
179 (Supplementary Table S.3). All the titanite analyses can be divided into two groups: (1)
180 Group I, with a $(HREE > LREE)_{chondrite}$ pattern; and (2) Group II, with a LREE-rich
181 pattern (Fig. 5b). Compared with Group II, Group I also shows relatively lower Th (10s
182 of ppb vs. several to 10s of ppm), U (several ppm vs. 10s to 100s of ppm), Pb (several
183 ppm vs. ~ 10s ppm), Sr (10s ppm vs. ~ 100s ppm) and L-MREE contents (several ppm
184 vs. ~ 10s ppm). Group I with a $(HREE > LREE)_{chondrite}$ pattern only represents the core
185 composition of the large titanite crystals from the metabasite, although some analyzed
186 spots of titanite core from the metabasite can also show LREE-rich feature.

187 **Phengite** contains the highest Ba, Rb and Cs (~ 10^3 ppm, 10^2 ppm and several ppm
188 respectively) among all the analyzed minerals (Fig. 5c). **Paragonite** also contains high
189 Ba-Rb-Pb-Sr, i.e., ~ 10 – 10^2 times the chondritic values to different extents (Fig. 5d).
190 Paragonite from the marble shows the lowest Sr contents than other paragonite crystals

191 (~ 100 ppm vs. ~ 300 – 500 ppm; Supplementary Table S.3). **Apatite** shows consistently
192 high Th, U, REEs, and Sr (~ 10^2 times the chondritic value) as well as some Pb (10
193 times the chondritic value; Fig. 5e). All the **omphacite** analyses show similarly low
194 contents of all the analyzed trace elements, except for Th, U and Sr (no more than 10
195 times the chondritic values; Fig. 5f). The Sr contents of omphacite from the marble
196 seem to be lower than those of other analyzed omphacite, 8.09 – 16.1 ppm vs. 19.7 ppm
197 (Supplementary Table S.3).

198 # 5 Discussions

199 ## 5.1 Controls on mineral compositional variations

200 All the above mineral trace element systematics (Fig. 5) generally confirm previous
201 studies (e.g., Tribuzio et al., 1996; Sorensen et al., 1997; Spandler et al., 2003; El Korh
202 et al., 2009; Hermann and Rubatto, 2009; Xiao et al., 2013, 2014). However, Sr contents
203 of omphacite from the marble (e.g., Figs. 3c,d) are lower than those of omphacite from
204 the metabasite and from subduction-zone metamorphosed rocks in our previous studies
205 for the Chinese Western Tianshan orogenic belt (8.09 – 16.1 ppm vs. up to 135 ppm;
206 Xiao et al., 2014). Paragonite from the marble (e.g., Fig. 3e) also shows the lowest Sr
207 contents among all the analyzed paragonite grains in this study, which are as low as
208 those of paragonite inclusions that together with clinozoisite occur as lawsonite
209 pseudomorphs in our previous studies (Xiao et al., 2014). Given the fact that calcite has
210 the great potential to host Sr, e.g., ~ 10^3 ppm (Spandler et al., 2003), lower Sr contents
211 of silicate minerals (omphacite and paragognite) from the marble is likely resulting

212 from the strong partitioning of Sr to the host marble. REE contents of epidote from the
213 marble (e.g., Figs. 3f, 5a) are significantly higher than those of (clino)zoisite from the
214 metabasite. The higher REE contents of epidote from the marble likely reflect the
215 stronger preference of REEs for epidote relative to calcium carbonate. In addition,
216 unlike the high $(LREE/HREE)_{chondrite}$ of analyzed clinozoisite from the metabasite and
217 other epidote from the marble, the high $(HREE/LREE)_{chondrite}$ of epidote overgrown on
218 the rim of garnet from the marble (Fig. 3b) clearly reflects the inheritance of HREEs
219 from garnet (Fig. 5a), indicating the significant re-distribution of REEs between
220 different mineral phases rather than their loss (Xiao et al., 2016).

221 As a major element for titanite, Ti contents of titanite are constrained by the
222 stoichiometry (i.e., $CaTiSiO_5$), but trace element contents of titanite are highly
223 heterogeneous, i.e., different spots show variable LREEs, Th, and U contents (Fig. 5b).
224 The significant correlations of U with the immobile elements (e.g., Th; Fig. 6a) and the
225 significant correlation of LREE (e.g., La) with the immobile elemental ratio (e.g.,
226 Th/Nb ratio; Fig. 6b) indicate that variations of LREEs, Th, and U in titanite are not
227 caused by the mobilization of these elements. Given the consistent Nb-Ta contents in
228 both of the two titanite groups, the obviously lower LREE-Th-U contents of the HREE-
229 rich titanite group than those of the LREE-rich titanite group reflects less LREE-Th-U
230 available for the growth of the HREE-rich titanite at the analyzed spots. Indeed, many
231 trace elements are only redistributed locally among different mineral phases with
232 metamorphic reactions (e.g., REEs redistributed from garnet to epidote group minerals
233 as discussed above; Xiao et al., 2014); heterogeneous trace element contents of

metamorphic minerals are controlled by the availability of their "compatible" trace elements (Xiao et al., 2016). Thus, the inherited both bulk rock and precursor mineral compositions and the competition between the adjacent growing minerals in contact can significantly affect trace element contents of metamorphic minerals. Because garnet prefers HREEs and epidote group minerals prefer LREEs, two different trace element patterns of titanite (Fig. 5b) reflect their inheritance from different precursor minerals (garnet vs. epidote). The inherited "garnet" trace element signature in high HREE group titanite offers evidence for complete transformation of garnet in the metabasite sample without garnet. Alternatively, considering the large amounts of clinozoisite in the metabasite and its significance for LREE-Th-U budget (Xiao et al., 2014), the growth of clinozoisite may also strongly result in the LREE-Th-U depletion of the neighboring titanite in contact (shown as Group I titanite).

5.2 Formation of the titanite-rich contact

The large titanite crystals as well as other titanite crystals at the titanite-rich contact between the marble and metabasite contain Nb and Ta as high as rutile. Tiny residual rutile remains in some large titanite crystals (Figs. 4d,e), probably resulting from the following reaction:

$$Rt + Coe/Qz + Arg/Cal \Rightarrow Ttn + CO_2 \uparrow \quad (1)$$

($TiO_2 + SiO_2 + CaCO_3 \Rightarrow CaTiSiO_5 + CO_2$; Niu and Lesher, 1991)

Furthermore, the lithological contact has been proposed to preferentially serve as the major conduit for the fluid flow (Breeding et al., 2003; Fig. 7). The orientation (i.e., parallel to the contact between the metabasite and marble), the large crystal size and the

256 abundant titanite at the titanite-rich contact emphasize its formation through the
257 metamorphic reaction between the two lithologies facilitated by SiO_2-rich fluids. The
258 absence of phengite and paragonite (the most important mineral hosts for highly water-
259 soluble LILEs and fluids; Xiao et al., 2014) at the titanite-rich contact between the two
260 lithologies suggests that highly water-soluble elements must have been largely
261 transported away with the fluids, and only immobile elements like Ti-Nb-Ta remain
262 stabilized in the form of titanite in the fluid conduit after dehydration and decarbonation.
263 As no obvious change of hydrous mineral modal abundances in metabasite and the
264 LILEs depletion in the titanite-rich contact, the fluids facilitating the reaction 1 are
265 unlikely derived from the metabasite or externally from the metasedimentary rocks.
266 The fluids externally derived from the subducting serpentinite (uppermost mantle
267 section of the slab equivalent to the "abyssal peridotites"; Niu, 2004), which can
268 continuously dehydrate to depths even up to ~ 250 km in cold subduction zones
269 (depending on the thermal structure of the slab; Syracuse et al., 2010), is more likely
270 responsible for this reaction.

271 The replacement of rutile by titanite is commonly thought to represent the
272 retrograde metamorphic process during the slab exhumation (e.g., Chen and Zheng,
273 2015; Zhang et al., 2016). However, the replacement during the apparent "retrograde"
274 metamorphism can actually happen with the change of geochemical composition of the
275 system (Fig. 7a) rather than with the decrease of pressure or temperature. Considering
276 the effects of CO_2 activity on the varying stability of titanite (Ye et al., 2002), titanite
277 instead of rutile can become stable at higher pressures in the system with decreasing

278 X_{CO2} (Fig. 7a). In addition, the titanite-rich contact in this study represents an open
279 system, possibly affected by externally derived fluids from the subducting serpentinite
280 and releasing CO_2 as well as other water-soluble elements via the reaction 1 as
281 discussed above. As a result, the release of CO_2 may further enhance the formation of
282 titanite, which can be formed even up to UHPM conditions (Ye et al., 2002; Lü et al.,
283 2013). In that case, carbonates (metamorphosed to eclogite-facies marble) participate
284 in the reaction with the metabasite during SZM at the lithological contact facilitated by
285 the fluid flow (Breeding et al., 2003). HFSEs can be hosted by and stabilized in the
286 newly formed titanite, while the fluid-soluble LILEs are readily transported away (e.g.,
287 to the mantle wedge) during subduction-zone dehydration metamorphism. Therefore, it
288 is important to emphasize that if the titanite can be formed and stable under UHPM
289 conditions, possibly by fluid-facilitated decarbonation reactions, it can host and
290 stabilize HFSEs in the oceanic crust passing through SZM, contributing to the
291 characteristic “arc signature” unique to subduction-zone magmatism (i.e., high LILEs,
292 low HFSEs).

293 **5.3 Geodynamic significance**

294 Globally, the distribution of subducting sedimentary carbonates is highly variable
295 from one trench to another (Plank and Langmuir, 1998). As Morse et al. (2007)
296 summarized, most sedimentary carbonate minerals deposited on the seafloor is of
297 biogenic origin (e.g., skeletal organisms such as corals, calcareous algae), rather than
298 of abiogenesis (mostly as sedimentary cements or through post-depositional reactions).
299 Hence, the occurrence of marine sedimentary carbonates is always related to the growth

300 of these organisms, which always prefer a warm environment, i.e., tropical and
301 subtropical zones between ~ 30°N and ~ 30°S. Correspondingly, subduction of marine
302 carbonates is more likely restricted to relatively lower latitude.

303 The palaeogeographic distribution of the North Tianshan during the Early
304 Carboniferous (~ 330 Ma) is located at the latitude of ~ 30°N or even lower as
305 evidenced by palaeomagnetic studies (Kirscher et al., 2014; Kirscher, 2015), and the
306 ancient South Tianshan Ocean was situated south of ~ 30°N, which is also supported
307 by the occurrence of abundant carbonates in the Chinese Western Tianshan orogenic
308 belt (Lü et al., 2013). Furthermore, because calcium carbonate dissolves at depths
309 deeper than the carbonate compensation depths (CCDs), and because all trenches are
310 deeper than the CCDs, subduction of carbonates requires silicate mix to enable
311 carbonate protected from the seawater. The forearc basin flysch caused by turbidity
312 currents from shallower depths can result in the presence of deep sea carbonates to
313 subduct (e.g., Ericson et al., 1952; Yamamoto et al., 1988; Tsuboi et al., 2014). Globally
314 heterogeneous distribution of carbonates from one trench to another makes it not
315 straightforward at present to quantify this process and geochemical consequences of
316 carbonate subduction. However, the observations and analysis we present here points
317 to the significance of subducting carbonates in moderating geochemical behaviors of
318 chemical elements during SZM, hence in improved understanding of geochemical
319 consequences of SZM, about which further research is warranted.

320 Recent studies (e.g., Castillo, 2015) have mentioned that as a result of precipitation
321 from seawater with abundant U but low Pb (> 1 ppm vs. 0.003 ppb), marine carbonates

are expected to show high U/Pb ratios. Together with the lowest Rb/Sr ratio of marine carbonates among other crustal rocks, he proposed that the subduction of ancient marine carbonates can result in characteristically high $^{238}U/^{204}Pb$ ratio (μ; HIMU) but unradiogenic $^{87}Sr/^{86}Sr$ isotopic signatures in OIB (Castillo, 2015). Based on significant correlations of U and Th with immobile elements (e.g., HFSEs) for subduction-zone metamorphosed rocks and IAB in our previous studies (Xiao et al., 2012, 2016), we think that U and Th are immobile or much less mobile than Pb during SZM. Although Sr and Rb are both mobilized during SZM as discussed in our previous studies (Xiao et al., 2012, 2016), Sr can be largely hosted by subducting carbonates. Hence, these different behaviors of radioactive parent and radiogenic daughter during SZM can result in the low U/Pb ratios but high Rb/Sr ratios of the released fluids. After being affected by these released fluids from the carbonate-bearing subducting slab during SZM, the mantle wedge as the source of IAB may also have lower U/Pb ratio and higher Rb/Sr ratio. This is consistent with the lower U/Pb but higher Rb/Sr ratios in IAB relative to MORB (e.g., the average values of U/Pb and Rb/Sr ratios for IAB are 0.1 and 0.04 compared with 0.19 and 0.02 in MORB; IAB data is referred to Elliott, 2003, and MORB data referred to Niu and Batiza, 1997). The high Rb/Sr but low U/Pb in the overlying mantle wedge can further evolve to high radiogenic $^{87}Sr/^{86}Sr$ and unradiogenic Pb isotopic features of EMI with time.

In addition, based on the petrological and geochemical studies of subducted marble from the Eocene Cycladic subduction complex on Syros and Tinos islands, Greece, Ague and Nicolescu (2014) reported abundant CO_2 release at the lithological contact

between metacarbonate and other lithologies (e.g., mantle rocks, blueschist or metapelites in the subduction channel along slab-mantle interfaces). However, instead of decarbonation reactions, these authors prefer a model of fluid-induced dissolution of calcium carbonate for CO_2 release, and they proposed that the water activity will be lowered by adding CO_2 to the fluids after the dissolution of $CaCO_3$ at high pressures. As a result, silicate minerals will precipitate owning to their lower solubility. Whether subducting carbonates undergo decarbonation or dissolution, the fluid infiltration along the lithological contact is crucial for the CO_2 release from the subducting slab. Considering the complex scenarios of the slab-mantle interface (Bebout, 2007a), i.e., different types of blocks with highly variable and hybridized compositions (including marble, other meta-sediments like metapelite, metabasite, and mantle peridotite), the decarbonation/dissolution of carbonate facilitated by fluids at the lithological contact during SZM (Fig. 7) is expected to be common (e.g., reaction 1 or see model of Ague and Nicolescu, 2014), and can release abundant CO_2 for global carbon cycling through arc volcanic degassing (e.g., Kerrick, 2001).

6 Conclusions

The titanite-rich contact between the marble and metabasite from the Chinese Western Tianshan UHPM belt provides important information on geochemical behaviors of chemical elements affected by subducting carbonates. The titanite-rich contact is formed as the result of decarbonation reaction between the two lithologies at the presence of SiO_2-rich fluids. Such reactions and products are expected to be common in subduction zones, and the release of CO_2 during this process can contribute

366 to the global carbon cycling. Importantly, this decarbonation reaction forms and
367 stabilizes titanite that preferentially conserves HFSEs over LILEs. Although globally
368 heterogeneous distribution of carbonates from one trench to another makes it not
369 straightforward at present to quantify this process and geochemical consequences of
370 SZM, serious effort is in urgent need because such processes may be fundamentally
371 important towards our improved understanding of subduction-zone magmatism and the
372 geochemical consequences of SZM.

373 ## Acknowledgements

374 This study was supported by the National Natural Science Foundation of China
375 (Grant numbers: 41572047 to Yuanyuan Xiao; 9101400, 41130314 to Yaoling Niu) and
376 the Excellent Young Project of Institute of Oceanology, Chinese Academy of Sciences
377 (Y52221101Q) and the Special Research Program of the State Oceanic Administration
378 of China (GASI-GEOGE-02) to Yuanyuan Xiao. We thank all the research staff in the
379 Institute of Earth Sciences, Academia Sinica, Taiwan, especially people from well-
380 communicated geochemical group for their great supports. We also thank Mr Yu-Shiang
381 Wang, Ms Hui-Ho Hseih, Mr Fulong Lin, and Ms Xiaohui Lin for their great helps on
382 geochemical analytical work. Professor M.F. Zhou, Professor J.H. Yang, Professor Y.L.
383 Xiao and an anonymous reviewer are greatly appreciated for their handling and
384 constructive suggestions. Detailed discussion with Dr. Guodong Wang is also helpful.

385 ## References

386 Ague, J.J., Nicolescu, S., 2014. Carbon dioxide released from subduction zones by fluid-mediated
387 reactions. Nature Geoscience 7, 355-360.
388 Ai, Y.L., Zhang, L.F., Li, X.P., Qu, J.F., 2006. Geochemical characteristics and tectonic implications of

HP-UHP eclogites and blueschists in Southwestern Tianshan, China. Progress in Natural Science 16, 624 - 632.

Ayuso, R., Tucker, R., Peters, S., Foley, N., Jackson, J., Robinson, S., Bove, M., 2013. Preliminary radiogenic isotope study on the origin of the Khanneshin carbonatite complex, Helmand Province, Afghanistan. Journal of Geochemical Exploration 133, 6-14.

Bebout, G.E., 2007a. Metamorphic chemical geodynamics of subdution zones. Earth and Planetary Science Letters 260, 373-393.

Beinlich, A., Klemd, R., John, T., Gao, J., 2010. Trace-element mobilization during Ca-metasomatism along a major fluid conduit: Eclogitization of blueschist as a consequence of fluid–rock interaction. Gechimica et Cosmochimica Acta 74, 1892-1922.

Biellmann, C., Gillet, P., Guyot, F.o., Peyronneau, J., Reynard, B., 1993. Experimental evidence for carbonate stability in the Earth's lower mantle. Earth and Planetary Science Letters 118, 31-41.

Breeding, C.M., Ague, J.J., Bröcker, M., Bolton, E.W., 2003. Blueschist preservation in a retrograded, high-pressure, low-temperature metamorphic terrane, Tinos, Greece: Implications for fluid flow paths in subduction zones. Geochemistry Geophysics Geosystems 4.

Caciagli, N., Manning, C., 2003. The solubility of calcite in water at 6–16 kbar and 500–800 °C. Contributions to Mineralogy and Petrology 146, 275-285.

Castillo, P.R., 2015. The recycling of marine carbonates and sources of HIMU and FOZO ocean island basalts. Lithos 216, 254-263.

Chen, Y.-X., Zheng, Y.-F., 2015. Extreme Nb/Ta fractionation in metamorphic titanite from ultrahigh-pressure metagranite. Geochimica et Cosmochimica Acta 150, 53-73.

Coleman, R.G., Lee, D.E., Beatty, L.B., Brannock, W.W., 1965. Eclogites and Eclogites: Their differences and similarities. Geological Society of Ameirca Bulletin 76, 483-508.

Dasgupta, R., Hirschmann, M.M., 2006. Melting in the Earth's deep upper mantle caused by carbon dioxide. Nature 440, 659-662.

Dasgupta, R., Hirschmann, M.M., 2010. The deep carbon cycle and melting in Earth's interior. Earth and Planetary Science Letters 298, 1-13.

El Korh, A., Schmidt, S.T., Ulianov, A., Potel, S., 2009. Trace element partitioning in HP-LT metamorphic assemblages during subduction-related metamorphism, Ile de Groix, France: a detailed LA-ICPMS Study. Journal of Petrology 50, 1107-1148.

Flesia, C., Frezzotti, M.L., 2015. The dilemma of the dwarf Earth's CO2 degassing: Irrelevant or crucial? Journal of Geochemical Exploration 152, 118-122.

Frezzotti, M.L., Selverstone, J., Sharp, Z.D., Compagnoni, R., 2011. Carbonate dissolution during subduction revealed by diamond-bearing rocks from the Alps. Nature Geoscience 4, 703-706.

Gao, J., John, T., Klemd, R., Xiong, X.M., 2007. Mobilization of Ti-Nb-Ta during subduction: Evidence from rutile-bearing dehydration segregations and veins hosted in eclogite, Tianshan, NW China. Geochimica et Cosmochimica Acta 71, 4974-4996.

Gao, J., Klemd, R., 2001. Primary fluids entrapped at blueschist to eclogite transition: evidence from the Tianshan meta-subduction complex in northwestern China. Contributions to Mineralogy and Petrology 142, 1-14.

Gao, J., Klemd, R., 2003. Formation of HP-LT rocks and their tectonic implications in the western Tianshan Orogen, NW China: geochemical and age constraints. Lithos 66, 1-22.

Gao, J., Klemd, R., Zhang, L., Wang, Z., Xiao, X., 1999. P-T path of high-pressure/low-temperature rocks and tectonic implications in the western Tianshan Mountains, NW China. Jounal of

433 Metamorphic Geology 17, 621-636.
434 Gorman, P.J., Kerrick, D.M., Connolly, J.A.D., 2006. Modeling open system metamorphic decarbonation
435 of subducting slabs. Geochemistry, Geophysics, Geosystems 7.
436 Hayes, J.M., Waldbauer, J.R., 2006. The carbon cycle and associated redox processes through time.
437 Hermann, J., 2003. Carbon recycled into deep Earth: Evidence from dolomite dissociation in subduction-
438 zone rocks: comments. Geology 31, e4-e5.
439 Hermann, J., Rubatto, D., 2009. Accessory phase control on the trace element signature of sediment
440 melts in subduction zones. Chemical Geology 265, 512-526.
441 Huybers, P., Langmuir, C., 2009. Feedback between deglaciation, volcanism, and atmospheric CO2.
442 Earth and Planetary Science Letters 286, 479-491.
443 John, T., Klemd, R., Gao, J., Garbe-Schonberg, C.D., 2008. Trace-element mobilization in slabs due to
444 non steady-state fluid-rock interaction: Constraints from an eclogite-facies transport vein in
445 blueschist (Tianshan, China). Lithos 103, 1-24.
446 Kerrick, D.M., 2001. Present and past nonanthropogenic CO2 degassing from the solid earth. Reviews
447 of Geophysics 39, 565-585.
448 Kerrick, D.M., Connolly, J.A.D., 2001a. Metamorphic devolatilization of subducted marine sediments
449 and the transport of volatiles into the Earth's mantle. Nature 411, 293-296.
450 Kerrick, D.M., Connolly, J.A.D., 2001b. Metamorphic devolatilization of subducted oceanic metabasalts:
451 implications for seismicity, arc magmatism and volatile recycling. Earth and Planetary Science
452 Letters 189, 19-29.
453 Kirscher, U., 2015. Paleozoic Paleogeography of the South Western Part of the Central Asian Orogenic
454 Belt - Paleomagnetic Constraints. Ludwig-Maximilians-Universität München, München, p. 142.
455 Kirscher, U., Bilardello, D., Mikolaichuk, A., Bachtadse, V., 2014. Correcting for inclination shallowing
456 of early Carboniferous sedimentary rocks from Kyrgyzstan—indication of stable subtropical
457 position of the North Tianshan Zone in the mid-late Palaeozoic. Geophysical Journal International
458 198, 1000-1015.
459 Lü, Z., Bucher, K., Zhang, L., 2013. Omphacite-bearing calcite marble and associated coesite-bearing
460 pelitic schist from the meta-ophiolitic belt of Chinese western Tianshan. Journal of Asian Earth
461 Sciences 76, 37-47.
462 Lü, Z., Zhang, L., 2012. Coesite in the eclogite and schist of the Atantayi Valley, southwestern Tianshan,
463 China. Chinese Science Bulletin 57, 1467-1472.
464 Lü, Z., Zhang, L., Chen, Z., 2014. Jadeite- and dolomite-bearing coesite eclogite from western Tianshan,
465 NW China. European Journal of Mineralogy 26, 245-256.
466 Lü, Z., Zhang, L.F., Du, J.X., Bucher, K., 2008. Coesite inlusions in garnet from eclogitic rocks in
467 western Tianshan, northwest China: Convincing proof of UHP metamorphism. American
468 Mineralogist 93, 1845-1850.
469 Lü, Z., Zhang, L.F., Du, J.X., Bucher, K., 2009. Petrology of coesite-bearing eclogite from Habutengsu
470 Valley, western Tianshan, NW China and its tectonometamorphic implication. Journal of
471 Metamorphic Geology 27, 773-787.
472 Leake, B.E., Woolley, A.R., Arps, C.E.S., Birch, W.D., Gilbert, M.C., Grice, J.D., Hawthorne, F.C., Kato,
473 A., Kisch, H.J., Krivovichev, V.G., Linthout, K., Laird, J., Mandarino, J.A., Maresch, W.V., Nickel,
474 E.H., Rock, N.M.S., Schumacher, J.C., Smith, D.C., Stephenson, N.C.N., Ungaretti, L., Whittaker,
475 E.J.W., Youzhi, G., 1997. Nomenclature of amphiboles; Report of the Subcommittee on
476 Amphiboles of the International Mineralogical Association, Commission on New Minerals and

Mineral Names. American Mineralogist 82, 1019-1037.
Liu, Y., He, D., Gao, C., Foley, S., Gao, S., Hu, Z., Zong, K., Chen, H., 2015. First direct evidence of sedimentary carbonate recycling in subduction-related xenoliths. Scientific Reports 5.
Manning, C.E., Shock, E.L., Sverjensky, D.A., 2013. The Chemistry of Carbon in Aqueous Fluids at Crustal and Upper-Mantle Conditions: Experimental and Theoretical Constraints. Reviews in mineralogy and geochemistry 75, 109-148.
McCulloch, M.T., Gamble, J.A., 1991. Geochemical and geodynamicai constraints on subduction. Earth and Planetary Science Letters 102, 358-374.
Morimoto, N., 1989. Nomenclature of pyroxenes. Canadian Mineralogist 27, 143-156.
Morse, J.W., Arvidson, R.S., Lüttge, A., 2007. Calcium Carbonate Formation and Dissolution. Chemical Reviews 107, 342-381.
Niu, Y.L., Lesher, C.M., 1991. Hydrothermal Alteration of Mafic Metavolcanic Rocks and Genesis of Fe-Zn-Cu Sulfide Deposits, Stone Hill District, Alabama. Economic Geology and the Bulletin of the Society of Economic Geologists 86, 983-1001.
Niu, Y.L., 2004. Bulk-rock major and trace element compositions of abyssal peridotites: Implications for mantle melting, melt extraction and post-melting processes beneath mid-ocean ridges. Journal of Petrology 45, 2423-2458.
Niu, Y., 2009. Some basic concepts and problems on the petrogenesis of intra-plate ocean island basalts. Chinese Science Bulletin 54, 4148-4160.
Plank, T., Langmuir, C.H., 1998. The chemical composition of subducting sediment and its consequences for the crust and mantle. Chemical Geology 145, 325-394.
Poli, S., 2015. Carbon mobilized at shallow depths in subduction zones by carbonatitic liquids. Nature Geosci advance online publication.
Rubatto, D., Hermann, J., 2003. Zircon formation during fluid circulation in eclogites (Monviso, Western Alps): Implications for Zr and Hf budget in subduction zones. Geochimica et Cosmochimica Acta 67, 2173-2187.
Sorensen, S.S., Grossman, J.N., Perfit, M.R., 1997. Phengite-hosted LILE enrichment in eclogite and related rocks: Implications for fluid-mediated mass transfer in subduction zones and arc magma genesis. Journal of Petrology 38, 3-34.
Spandler, C., Hermann, J., Arculus, R., Mavrogenes, J., 2003. Redistribution of trace elements during prograde metamorphism from lawsonite blueschist to eclogite facies; implications for deep subduction-zone processes. Contributions to Mineralogy and Petrology 146, 205-222.
Sun, S.-s., McDonough, W.F., 1989. Chemical and isotopic systematics of oceanic basalts: implications for mantle composition and processes. Geological Society, London, Special Publications 42, 313-345.
Tanis, E.A., Simon, A., Zhang, Y., Chow, P., Xiao, Y., Hanchar, J.M., Tschauner, O., Shen, G., 2016. Rutile solubility in NaF–NaCl–KCl-bearing aqueous fluids at 0.5–2.79 GPa and 250–650 °C. Geochimica et Cosmochimica Acta 177, 170-181.
Thomson, A.R., Walter, M.J., Kohn, S.C., Brooker, R.A., 2016. Slab melting as a barrier to deep carbon subduction. Nature 529, 76-79.
Tribuzio, R., Messiga, B., Vannucci, R., Bottazzi, P., 1996. Rare earth element redistribution during high-pressure–low-temperature metamorphism in ophiolitic Fe-gabbros (Liguria, northwestern Italy): Implications for light REE mobility in subduction zones. Geology 24, 711-714.
Tsuboi, T., Wada, H., Nakamura, T., Hang, T.T., Matsuzaki, H., Otsuji, N., Fujioka, K., Oguri, K.,

Kitazato, H., 2014. Deep-sea limestone block as a source of 14C-depleted dissolved inorganic carbon at the Palau Trench. Chemical Geology 364, 1-8.

Tsuno, K., Dasgupta, R., Danielson, L., Righter, K., 2012. Flux of carbonate melt from deeply subducted pelitic sediments: Geophysical and geochemical implications for the source of Central American volcanic arc. Geophysical Research Letters 39.

Wilke, M., Schmidt, C., Dubrail, J., Appel, K., Borchert, M., Kvashnina, K., Manning, C.E., 2012. Zircon solubility and zirconium complexation in H2O+Na2O+SiO2±Al2O3 fluids at high pressure and temperature. Earth and Planetary Science Letters 349–350, 15-25.

Xiao, Y., Lavis, S., Niu, Y., Pearce, J.A., Li, H., Wang, H., Davidson, J., 2012. Trace-element transport during subduction-zone ultrahigh-pressure metamorphism: Evidence from western Tianshan, China. Geological Society of America Bulletin 124, 1113-1129.

Xiao, Y., Niu, Y., Li, H., Wang, H., Liu, X., Davidson, J., 2014. Trace element budgets and (re-)distribution during subduction-zone ultrahigh pressure metamorphism: Evidence from Western Tianshan, China. Chemical Geology 365, 54-68.

Xiao, Y., Niu, Y., Song, S., Davidson, J., Liu, X., 2013. Elemental responses to subduction-zone metamorphism: Constraints from the North Qilian Mountain, NW China. Lithos 160–161, 55-67.

Xiao, Y., Niu, Y., Wang, K.-L., Lee, D.-C., Iizuka, Y., 2016. Geochemical behaviours of chemical elements during subduction-zone metamorphism and geodynamic significance. International Geology Review 58, 1253-1277.

Yamamoto, S., Tokuyama, H., Fujioka, K., Takeuchi, A., Ujiié, H., 1988. Carbonate turbidites deposited on the floor of the Palau Trench. Marine Geology 82, 217-233.

Yaxley, G., Brey, G., 2004. Phase relations of carbonate-bearing eclogite assemblages from 2.5 to 5.5 GPa: implications for petrogenesis of carbonatites. Contributions to Mineralogy and Petrology 146, 606-619.

Ye, K., Liu, J.-B., Cong, B.-L., Ye, D.-N., Xu, P., Omori, S., Maruyama, S., 2002. Ultrahigh-pressure (UHP) low-Al titanites from carbonate-bearing rocks in Dabieshan- Sulu UHP terrane, eastern China, American Mineralogist, 875-881.

Zack, T., John, T., 2007. An evaluation of reactive fluid flow and trace element mobility in subducting slabs. Chemical Geology 239, 199-216.

Zhang, L.F., Ellis, D.J., Jiang, W.B., 2002a. Ultrahigh-pressure metamorphism in western Tianshan, China: Part I. Evidence from inclusions of coesite pseudomorphs in garnet and from quartz exsolution lamellae in omphacite in eclogites. American Mineralogist 87, 853-860.

Zhang, L.F., Ellis, D.J., Williams, S., Jiang, W.B., 2002b. Ultra-high pressure metamorphism in western Tianshan, China: Part II. Evidence from magnesite in eclogite. American Mineralogist 87, 861-866.

Zhang, L.J., Zhang, L.F., Lü, Z., Bader, T., Chen, Z., 2016. Nb–Ta mobility and fractionation during exhumation of UHP eclogite from southwestern Tianshan, China. Journal of Asian Earth Sciences 122, 136-157.

Supplementary Material

Supplementary data can be found in the online version of this article:

Supplementary Table S.1 Major element contents of minerals in sample 12TS-

AT-18 by using SEM-EDS.

Supplementary Table S.2 Analytical results of standard BCR-2G by using LA-ICP-MS.

Supplementary Table S.3 Trace element contents of minerals in sample 12TS-AT-18 by using LA-ICP-MS.

Supplementary Figure S.1 Mineral classification diagrams to show different mineral compositions. (a) Garnet classification, modified from Coleman et al. (1965). (b) Clinopyroxene classification, modified from Morimoto (1989), showing all the analyzed clinopyroxene in this study is omphacite. Q – quad, representing the Ca-Mg-Fe pyroxene area (Morimoto, 1989). (c) White mica classification, showing phengite and paragonite. (d-e) Amphibole classification, modified from Leake et al. (1997), showing amphibole analyzed are calcic or sodic-calcic. See explanations of mineral abbreviations in the caption of Fig. 3.

Figure Captions

Figure 1 Geological sketch of the Chinese Western Tianshan HP-UHP metamorphic terrane (Lü et al., 2013) and our sampling location for this study.

Figure 2 Photos of field observations along the Atantayi River. (a-b) Intercalated marble, mica schist and mica quartz schist without obvious deformation, reflecting the well-preserved flysch structure. The protolith of marble, mica schist and quartz schist are carbonate, pelite and sandstone respectively. Marble can also occur as boulders (b), the long axis of which is consistent with the orientation of foliation in

582 neighbouring rocks. (c) Metabasite boulders in marble. The dash lines represent the
583 folding foliation of carbonate turbidites (including some pelitic materials) as a result
584 of plastic deformation. (d) The metabasite occurs as enclaves in the marble host, the
585 contact of which is sampled (12TS-AT-18) in this study.

586 **Figure 3** Photomicrographs of sample 12TS-AT-18. The pink thick dash line represents
587 the titanite-rich contact between the marble and metabasite. (b-f), (g-h) and (i-l)
588 represent mineral assemblages in the marble, the titanite-rich contact and the
589 metabasite respectively. The length of the red line marked in each photo is
590 equivalent to 100 μm. Images (c, g, i-l) are taken under plane polarized light, and
591 the others are taken under cross polarized light. Mineral abbreviations used in this
592 study are as follows: Ab – albite; Ae – aegirine; Amp – amphibole; Ap – apatite;
593 Arg – aragonite; Ca – carbonate; Cal – calcium carbonate; Coe – coesite; Czs –
594 clinozoisite; Gln – glaucophane; Grt – garnet; Ep – epidote; Omp – omphacite; Pg
595 – paragonite; Ph – phengite; Qz – quartz; Rt – rutile; Ttn – titanite.

596 **Figure 4** Backscattered electron (BSE) images. (a-c) display the accessory minerals in
597 the marble. (d-e) show residual rutile in big titanite crystals from the metabasite and
598 the titanite-rich contact between the marble and metabasite. The thick black lines
599 or dots as indicated (MP, marking pen) are stained by marking pen when label. See
600 explanations of mineral abbreviations in the caption of Fig. 3.

601 **Figure 5** Chondrite (Sun and McDonough, 1989) normalized mineral trace element
602 abundances. (a) Epidote trace element pattern, with highly variable REEs contents.

603 The red lines represent compositions of epidote from the marble (e.g., Fig. 3f),
604 which contains the highest LREEs. It indicates the strongest preference of epidote
605 for LREEs than other minerals. The dotted lines represent compositions of epidote
606 overgrown on the rim of garnet from the marble (Fig. 3b). The trace element pattern
607 of the residual garnet is also plotted for comparison, represented by the line with
608 hollow circles. The similar trace element feature between the residual garnet and
609 the epidote rim clearly indicates the significant inheritance of HREEs from garnet
610 to epidote. (b) Two trace element patterns of titanite with different LREE/HREE
611 ratios. The HREE-rich pattern mostly represent the core composition of big titanite
612 crystals from the metabasite, while the LREE-rich pattern mostly represent titanite
613 from the titanite-rich contact and the rim composition of those from the metabasite.
614 (c-d) Phengite and paragonite trace element patterns, which are characterized by
615 high LILEs. (e) Apatite trace element pattern, showing consistently high Th-U-Sr-
616 REEs. (f) Omphacite trace element pattern, with only a little high U and Sr.

617 **Figure 6** Co-variation diagrams for titanite: (a) Th – U, (b) Th/La – Th/Nb. The two
618 groups of titanite with different LREE/HREE ratio patterns as shown in Fig. 5b are
619 also reflected as two groups in these figures, i.e., red solid circles (11 analyzed spots)
620 for the HREE-rich group representing the core composition of titanite from the
621 metabasite, while blue solid rectangles (49 analyzed spots) for the LREE-rich group
622 mostly representing titanite from the titanite-rich contact and the rim composition
623 of those from the metabasite. U (a) and LREE (represented by La; b) correlate with
624 the immobile Th and Nb (the critical values of Pearson's correlation coefficient

using one-tail test for 11 samples and 49 samples are 0.5214 and 0.2377 respectively at > 95% confidence levels), indicating that the variation of LREE-U in titanite are not caused by the mobility of these elements.

Figure 7 (a) P-T diagram showing phase equilibria of the reaction: Rt + Coe/Qz + Arg/Cal => Ttn + CO_2 ↑ (after Ye et al., 2002). Numbers at the end of the univariate curves are X_{CO2} values. The red solid circle represents the peak metamorphic condition of the Chinese Western Tianshan, i.e., ~ 520 °C at 2.7 GPa (Lü et al., 2009). It is below the univariate line with X_{CO2}=0.001 (in orange) but above the univariate line with X_{CO2}=0.01 (in blue), indicating titanite can become stable in the system with decreasing X_{CO2} rather than with decreasing pressure or temperature. (b) The schematic diagram for the context of the slab subduction, modified from Niu (2009). The released fluids and the hydrous melts (including supercritical fluids) derived from the subducting slab can carry certain elements into the overlying mantle wedge, and contribute to the petrogenesis of IAB. As a result, the composition of the altered subducting slab after SZM and hydrous melting into the deep mantle cannot be equal to the inputting composition into the trench. (c) The schematic diagram showing diverse lithologies with different mineral assemblages in the subduction channel (marble, other meta-sediments like metapelite, metabasite, peridotite, mélange matrix) and the fluid flow as well as the hydrous melts from the subducting slab (modified from Xiao et al., 2016). (d) The schematic diagram showing reactions between different lithologies, which are facilitated by infiltrated fluids along the lithological contact.

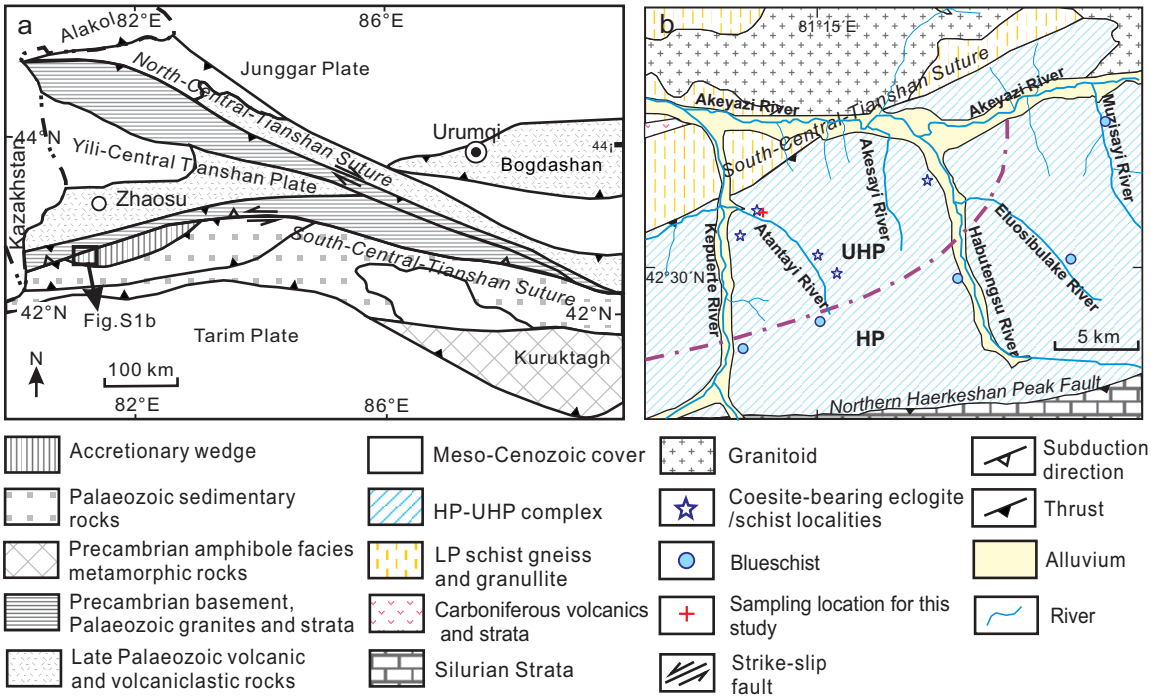
a
Alakol
82°E
86°E
Junggar Plate
North-Central-Tianshan Suture
Urumqi
Bogdashan
44°N
Yili-Central Tianshan Plate
Zhaosu
Kazakhstan
South-Central-Tianshan Suture
42°N
Fig.S1b
Tarim Plate
Kuruktagh
N
100 km
82°E
86°E
b
81°15′E
Akeyazi River
South-Central-Tianshan Suture
Akeyazi River
Muzisayi River
Akesayi River
Atantayi River
Kepuerte River
UHP
42°30′N
Habutengsu River
Eluosibulake River
HP
5 km
Northern Haerkeshan Peak Fault
Accretionary wedge
Palaeozoic sedimentary rocks
Precambrian amphibole facies metamorphic rocks
Precambrian basement, Palaeozoic granites and strata
Late Palaeozoic volcanic and volcaniclastic rocks
Meso-Cenozoic cover
HP-UHP complex
LP schist gneiss and granullite
Carboniferous volcanics and strata
Silurian Strata
Granitoid
Coesite-bearing eclogite /schist localities
Blueschist
Sampling location for this study
Strike-slip fault
Subduction direction
Thrust
Alluvium
River

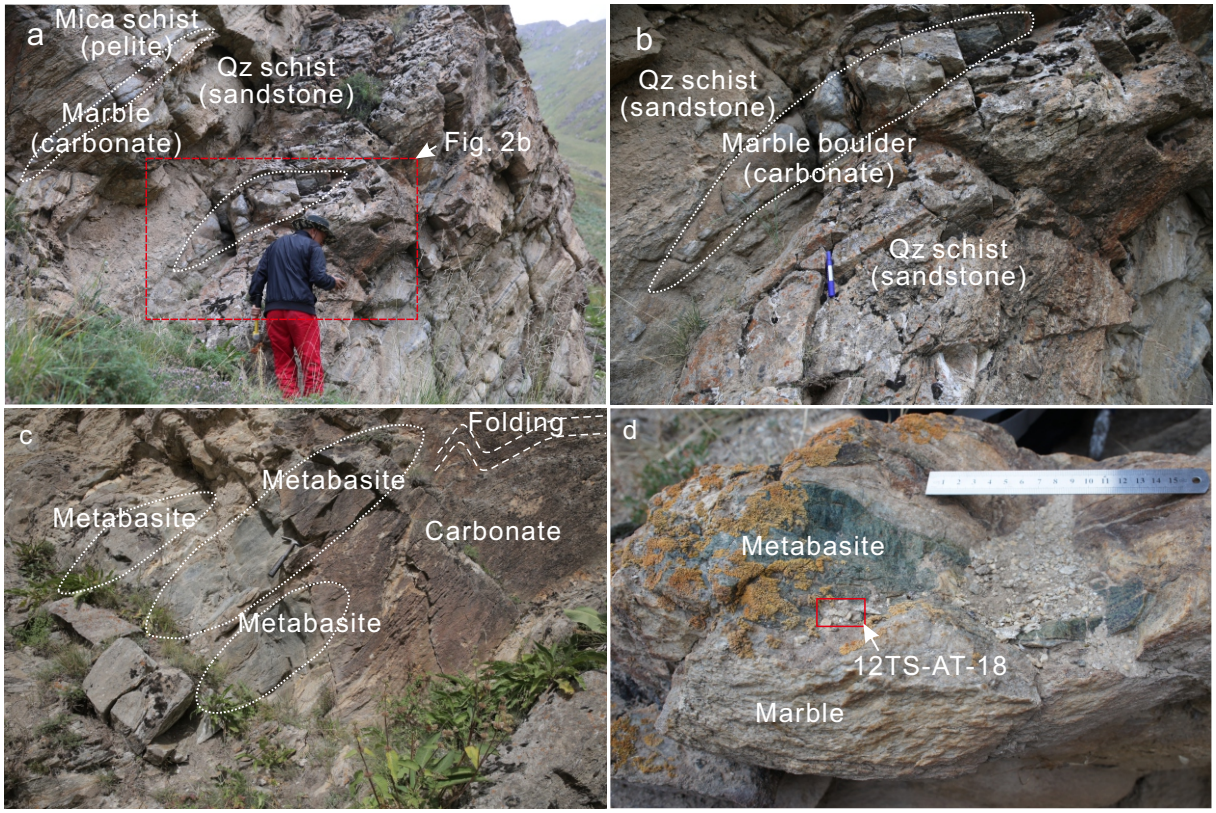
a
Mica schist
(pelite)
Qz schist
(sandstone)
Marble
(carbonate)
Fig. 2b
b
Qz schist
(sandstone)
Marble boulder
(carbonate)
Qz schist
(sandstone)
c
Folding
Metabasite
Metabasite
Carbonate
Metabasite
d
Metabasite
12TS-AT-18
Marble

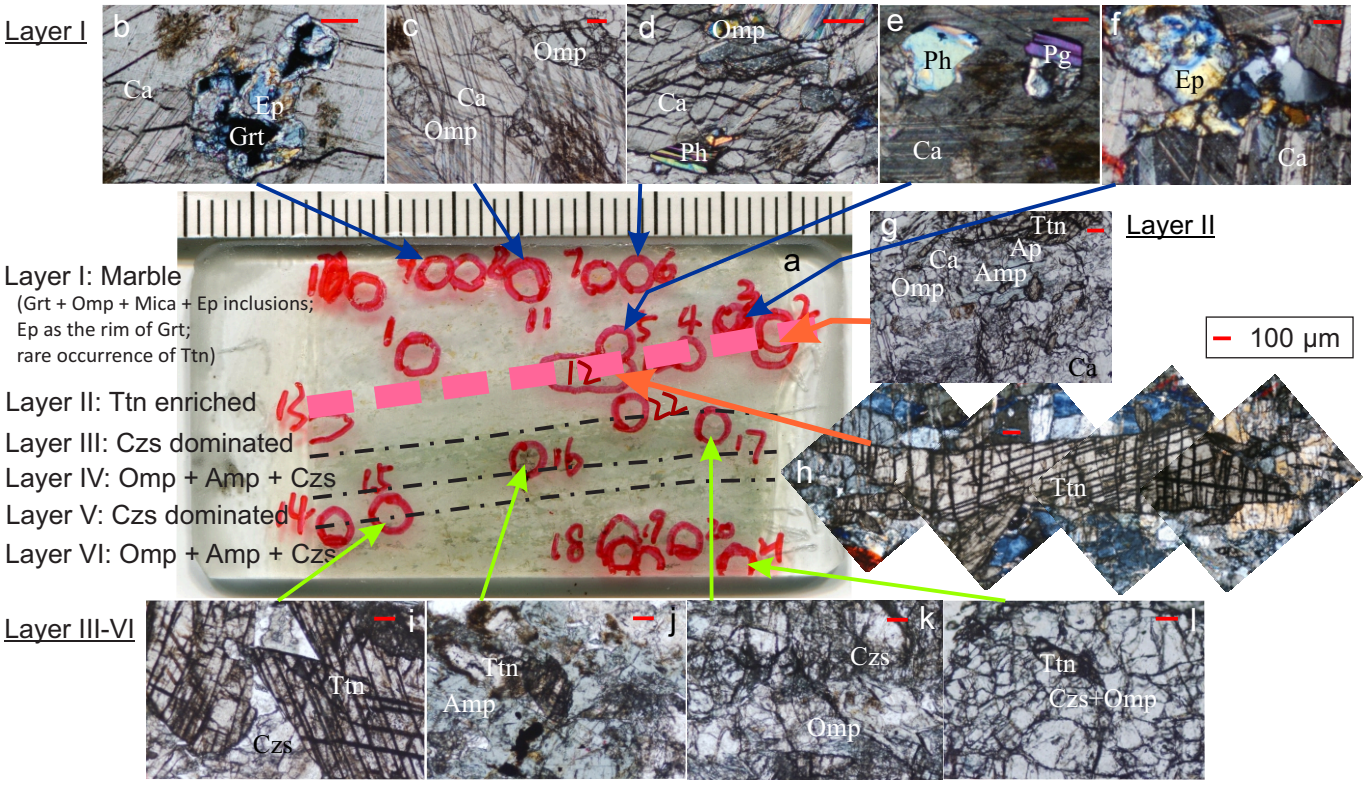
Layer I
b
Ca
Ep
Grt
c
Omp
Ca
Omp
d
Omp
Ca
Ph
e
Ph
Pg
Ca
f
Ep
Ca
a
g
Ttn
Ap
Ca
Amp
Omp
Ca
Layer II
100 µm
h
Ttn
Layer I: Marble
(Grt + Omp + Mica + Ep inclusions;
Ep as the rim of Grt;
rare occurrence of Ttn)
Layer II: Ttn enriched
Layer III: Czs dominated
Layer IV: Omp + Amp + Czs
Layer V: Czs dominated
Layer VI: Omp + Amp + Czs
Layer III-VI
i
Ttn
Czs
j
Ttn
Amp
k
Czs
Omp
l
Ttn
Czs+Omp

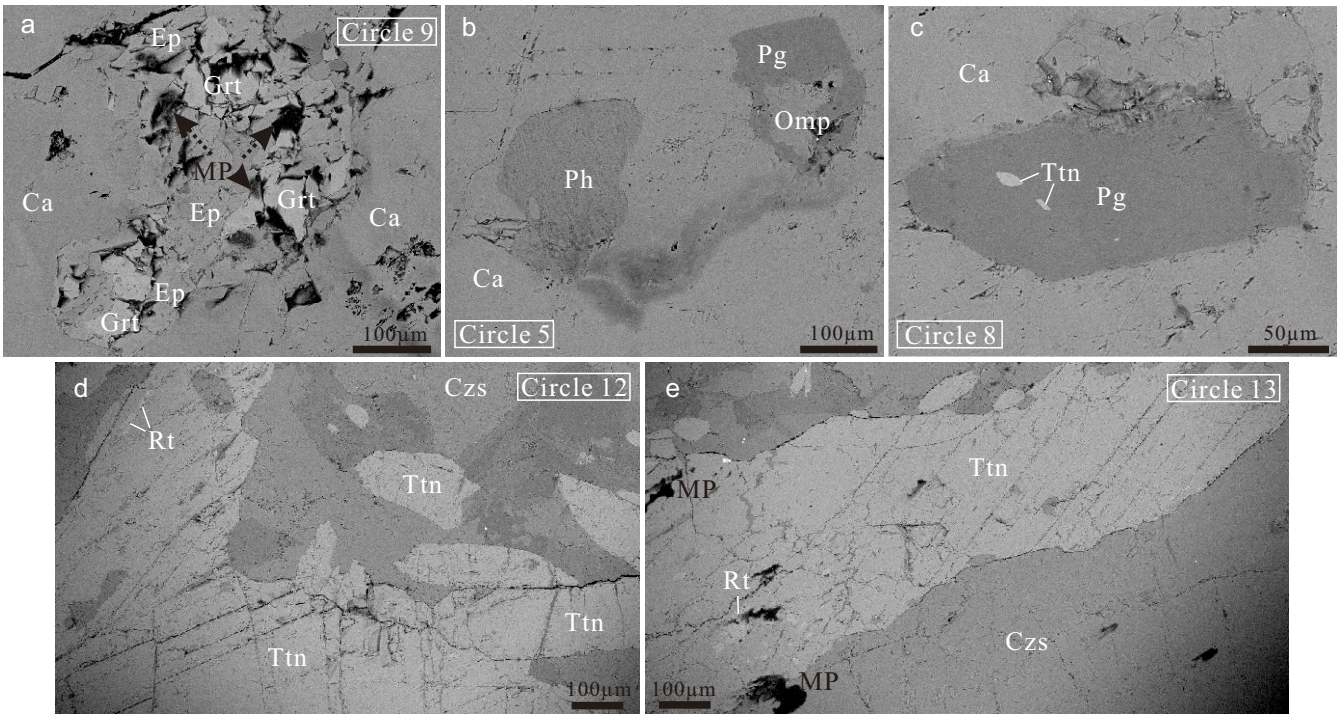
a
Circle 9
Ep
Grt
MP
Ca
Ep
Grt
Ca
Ep
Grt
100μm
b
Pg
Omp
Ph
Ca
Circle 5
100μm
c
Ca
Ttn
Pg
Circle 8
50μm
d
Czs
Circle 12
Rt
Ttn
Ttn
Ttn
100μm
e
Circle 13
Ttn
MP
Rt
Czs
100μm
MP

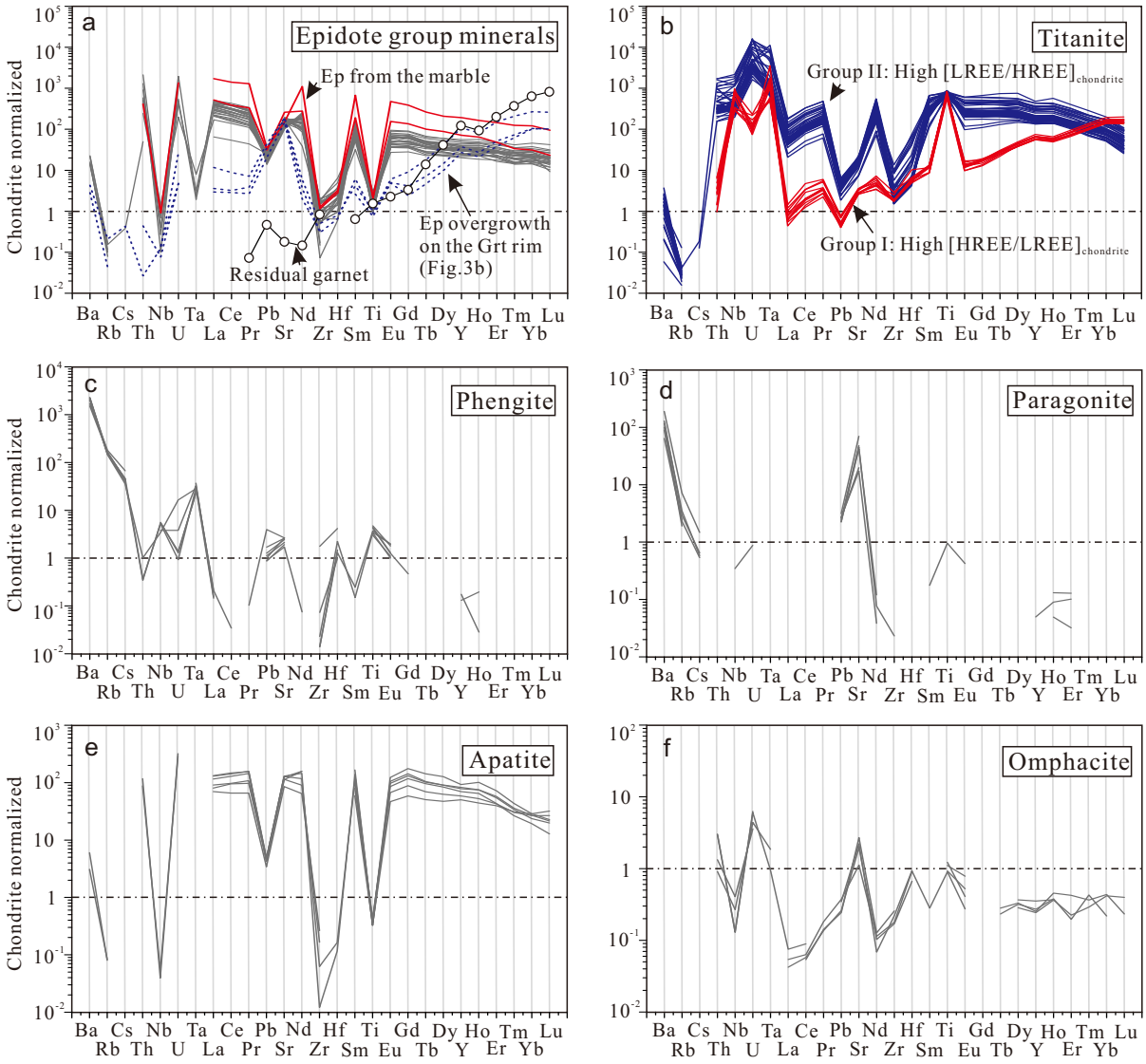
a
Epidote group minerals
Ep from the marble
Ep overgrowth on the Grt rim (Fig.3b)
Residual garnet
b
Titanite
Group II: High [LREE/HREE]chondrite
Group I: High [HREE/LREE]chondrite
c
Phengite
d
Paragonite
e
Apatite
f
Omphacite
Chondrite normalized
Ba Cs Nb Ta Ce Pb Nd Hf Ti Gd Dy Ho Tm Lu
Rb Th U La Pr Sr Zr Sm Eu Tb Y Er Yb

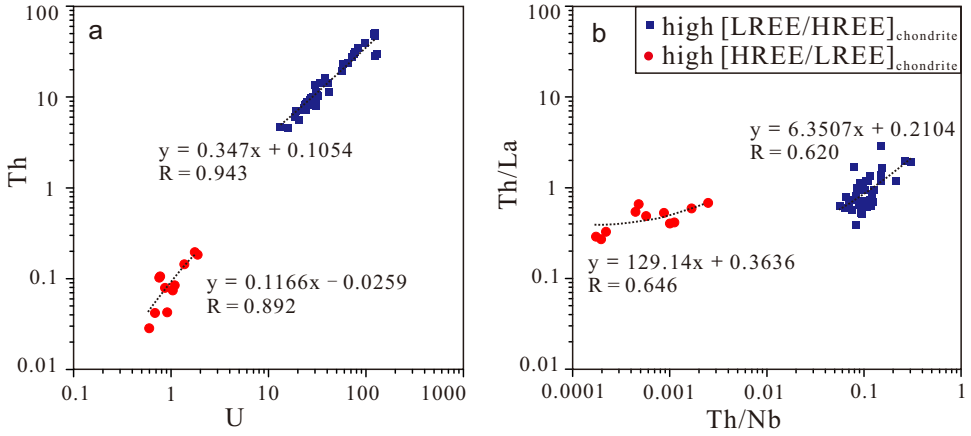
a
Th
U
y = 0.347x + 0.1054
R = 0.943
y = 0.1166x − 0.0259
R = 0.892
b
high [LREE/HREE]chondrite
high [HREE/LREE]chondrite
Th/La
Th/Nb
y = 6.3507x + 0.2104
R = 0.620
y = 129.14x + 0.3636
R = 0.646

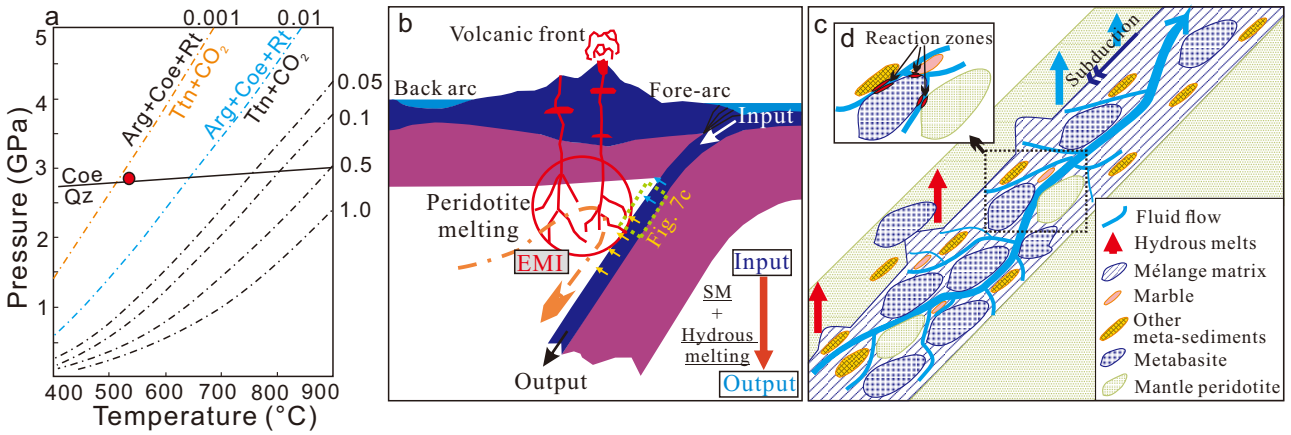
a
0.001
0.01
Arg+Coe+Rt
Ttn+CO2
Arg+Coe+Rt
Ttn+CO2
0.05
0.1
0.5
1.0
Coe
Qz
Pressure (GPa)
Temperature (°C)
b
Volcanic front
Back arc
Fore-arc
Input
Peridotite melting
EMI
Fig. 7c
Input
SM + Hydrous melting
Output
Output
c
d Reaction zones
Subduction
Fluid flow
Hydrous melts
Mélange matrix
Marble
Other meta-sediments
Metabasite
Mantle peridotite

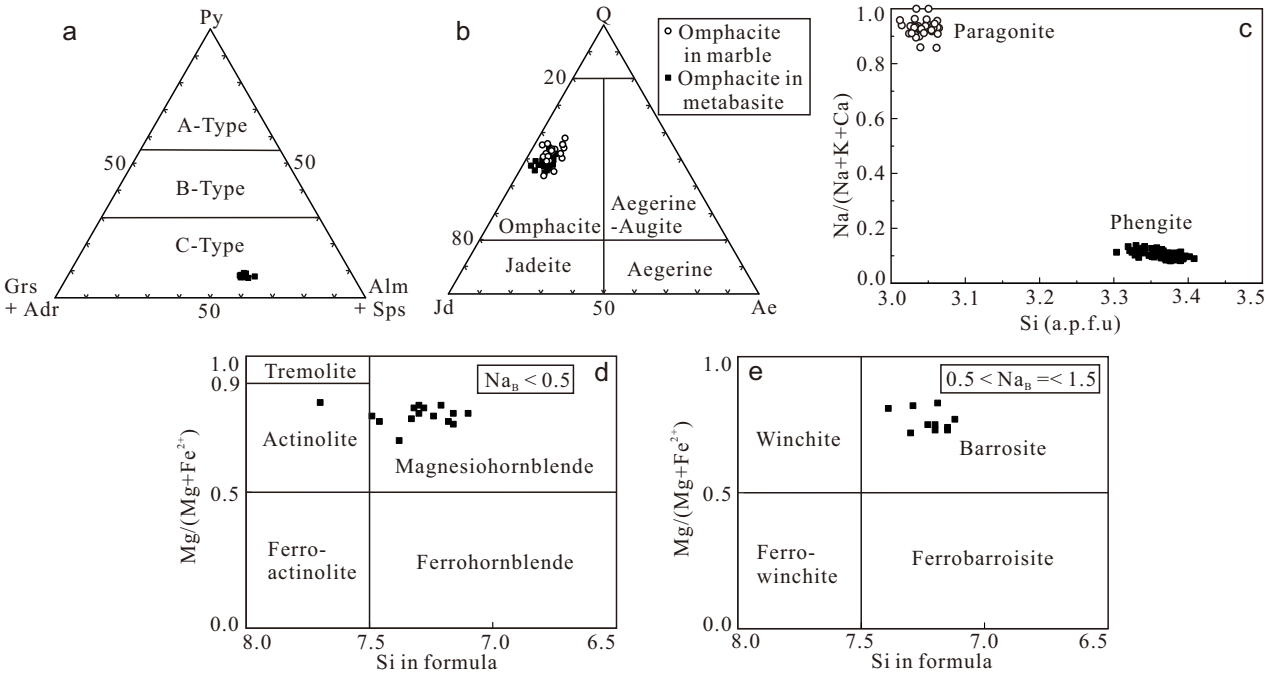
a
Py
A-Type
B-Type
C-Type
50
50
Grs
+ Adr
50
Alm
+ Sps
b
Q
Omphacite
in marble
Omphacite in
metabasite
20
80
Omphacite
Aegerine
-Augite
Jadeite
Aegerine
Jd
50
Ae
c
Paragonite
Phengite
Na/(Na+K+Ca)
Si (a.p.f.u)
d
Tremolite
Actinolite
Magnesiohornblende
Ferro-
actinolite
Ferrohornblende
Na$_B$ < 0.5
Mg/(Mg+Fe^{2+})
Si in formula
e
Winchite
Barrosite
Ferro-
winchite
Ferrobarroisite
0.5 < Na$_B$ =< 1.5
Mg/(Mg+Fe^{2+})
Si in formula